Omnidirectional droplet propulsion on surfaces with a Pac-Man coalescence mechanism

Jana Chaaban⬤, Patrick Galliker, Thomas M. Schutzius⬤,[*] and Dimos Poulikakos⬤[†]

Laboratory of Thermodynamics in Emerging Technologies, Department of Mechanical and Process Engineering, ETH Zurich, Sonneggstrasse 3, CH-8092 Zurich, Switzerland

Dispensing, transporting, and manipulating minute liquid volumes is important to a wide range of scientific and application areas, spanning from biology and medicine to chemistry and materials. Although digital microfluidics are emerging as a popular methodology in the lab-on-a-chip field, important obstacles to its broad adoption, such as those related to reusability, reconfigurability, and susceptibility to fouling, persist. In addition, as liquid volumes decrease in size, their sustenance in an open atmosphere becomes practically impossible due to high volatility, leading rapidly to complete evaporation. Here we introduce and demonstrate a microfluidic platform based on the coalescence-induced self-propulsion of sessile microdroplets on unpatterned substrates. We employ controlled dropwise liquid ejection by electrohydrodynamic printing to create, actively sustain (despite high volatility), and freely translate femtoliter-sized droplets ($\sim$2–5 μm radius) under open-atmosphere conditions. The omnidirectional planar movement of the droplets is achieved by a precisely controlled, on-demand sequence of coalescence events, where the directed motion of an already deposited droplet is dictated by the positioning of the subsequent droplet printed adjacent to it. We studied the transport mechanism experimentally and theoretically and found that, for short time scales (relative to the substrate translation and droplet evaporation), the radial growth of the new smaller droplet being printed can greatly exceed the retraction of the neighboring, already deposited droplet. This rapid growth is exploited to create a liquid meniscus bridging the so generated droplet doublet, and merging it into a single droplet by the action of capillary pressure differences. Evaporative losses ensure that the moving droplets are kept at a constant size after merging, in each coalescence cycle. We observe this coalescence whenever the interspacing between two sequentially printed droplets is below a critical value, and show that we can control this with the underlying substrate velocity. Armed with this transport mechanism, we then demonstrate the utility of this approach by tasking the coalescing self-propelled droplet doublet to perform microfluidic operations such as collecting, transporting, and merging solid residues on a surface, in an on-demand, Pac-Man type motion, exemplifying capabilities for digital microfluidic applications.

---

[*]Present address: ETH Zurich, Laboratory of Multiphase Thermofluidics and Surface Nanoengineering, Department of Mechanical and Process Engineering, CH-8092 Zurich, Switzerland; Corresponding author: thomschu@ethz.ch

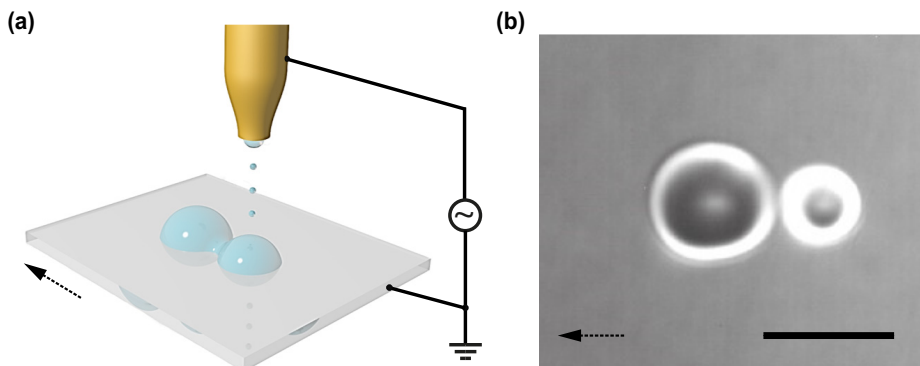[†]Corresponding author: dpoulikakos@ethz.ch

FIG. 1. Formation of a droplet pair: (a) Schematic of the droplet pair formation. The droplet pair is formed by shifting the nozzle-substrate axis (by moving the substrate) beyond the perimeter of the large, initial "mother" droplet. This leads to the formation of a "daughter," adjacent droplet, which grows through the continuous addition of printed smaller droplets by the nozzle. The pair reaches a quasiequilibrium state once the continuously added printed liquid equals evaporative losses of the pair. (b) Bottom view, optical micrograph of two adjacent sessile droplets formed by the process shown in (a), before coalescence. Scale bar: (b) 10 μm.

I. INTRODUCTION

Microfluidic handling techniques hold great promise for a plethora of applications, ranging from medicine and biology [1–4] to chemistry and materials synthesis and transport [5–7]. Droplet microfluidics offer unrivalled economy of scale, by drastically reducing waste production, while enhancing experiment integration and throughput [8–14]. In particular, digital microfluidics enable the programmable manipulation of microscale droplets, without the need for complex networks of channels, pumps, or microvalves [15–20]. Discrete droplets are manipulated by means of various fluidic actuators, including dielectrophoresis (DEP) [21–23], electrowetting on dielectrics (EWOD) [24–27], magnetic forces [28–30], and surface acoustic waves [31,32]. Droplet motion in such systems is often limited by the need for specific droplet properties and unwanted surface fouling. In the context of open-air platforms, the major challenge is the stabilization of microscopic droplets, which become ever more volatile as a result of their minute size, posing a lower size limit to droplet related applications. Moreover, the movement range of the droplets is often limited to a set number of configurable paths, owing to the limited space and electrode density on the predesigned substrate.

Here we introduce a unique surface microfluidics platform in which microscopic droplets are formed, actively sustained, individually addressed, and moved on-demand omnidirectionally on unpatterned substrates, under open-atmosphere conditions. The enabling propulsion mechanism relies on the controlled, serial coalescence of continuously printed sessile microdroplets—which we explore in-depth in this study—and the subsequent displacement of the resulting merged microdroplets. The sessile microdroplets are kept temporally stable, despite their size-induced high volatility, through continuous dropwise NanoDrip printing-based replenishment of liquid, to compensate for the quantity being lost through evaporation [Fig. 1(a)]. NanoDrip printing is a recently demonstrated form of electrohydrodynamic liquid ejection, capable of depositing discrete, ultrasmall liquid quantities down to the zeptoliter range, with nanoscopic placement precision [33–36]. NanoDrip printing has previously been used to create and actively counteract the evaporation of attoliter liquid droplets under normal atmospheric conditions, but has never been explored to transport droplets over a surface, as required for surface microfluidics [37].

In this work, we show that such artificially sustained droplets are not restricted to a fixed position on the underlying substrate, but can be made mobile in any planar direction by a continuous sequence of controlled coalescence events. Moreover, we employ the coalescing self-propelled droplet doublet, to controllably pick up, transport, and assemble preexisting solid particles on unpatterned

substrates. Whereas the coalescence of freely suspended droplets is a purely hydrodynamic process [38,39], the coalescence kinetics of sessile droplets is markedly influenced by the presence of the solid surface, and hence by the contact line motion itself [40,41]. With the presented platform, we experimentally investigate the fundamentals of the coalescence dynamics and motion of sessile microdroplets in a partially wetting regime. Based on theoretical and experimental observations, we also explore the limits of this coalescence-induced motion mechanism, and the conditions where this mode of transport can operate.

II. RESULTS AND DISCUSSION

A. Observation and theoretical analysis

We employed on demand dropwise liquid deposition by electrohydrodynamic nanoprinting, to additively create and sustain femtoliter sessile droplets in an open atmosphere, on unpatterned partially wetting surfaces. Propylene glycol n-butyl ether (PnB) was used as the solvent in the experiments, owing to its low vapor pressure—reducing evaporation—and sufficiently high electrical conductivity, allowing it to be printable. The droplets were deposited on borosillicate glass slip substrates coated with a self-assembled monolayer of 1H,1H,2H,2H-Perflurooctyltrichlorosilane (FDTS). We observed the droplets *in situ*, from below, by a laser scanning microscope. The accumulated sessile droplets enter a temporally stable, quasiequilibrated state when the ongoing addition of liquid matches the average liquid quantity lost through evaporation [37]. A simplified schematic of the printing setup is illustrated in Fig. 1(a). Once we move the nozzle symmetry axis beyond the geometric boundaries of the initial sessile droplet contact area, dubbed "mother" droplet, the ejection flow starts to accumulate adjacent to it, forming a new, smaller "daughter" droplet as illustrated in Fig. 1(b). As airborne droplets are continuously added to it, the daughter droplet grows to cover a larger contact area with the surface, and if it eventually contacts the mother droplet, capillarity drives coalescence of the two droplets. In the following, we use the same partially wetting substrate, and employ the same fixed printing parameters for all experiments.

The coalescence process is characterized by two distinct stages, based on the time evolution of the droplet shape [40–43]. A schematic representation of a typical coalescence cycle of a mother and a daughter droplet (droplets 1 and 2, respectively) is shown in a simplified manner, from a side-view perspective, in Fig. 2(a), and captured through optical micrographs, from a bottom-view perspective, in Fig. 2(b). Figure 2(b) shows the droplets 1 and 2 prior to bridging at $t = -4.24$ ms. Upon contact, a liquid meniscus forms and grows rapidly, in both perpendicular and parallel directions, bridging the two droplets [43,44]. At $t = 0$ the two droplets coalesce, forming an initially elongated composite droplet, number 3, concluding the first stage of the coalescence process. The composite droplet shape can be characterized by its large axis $2R_{3,y}$ measured in the direction of maximum elongation, and its small axis $2R_{3,x}$ measured in the perpendicular direction, as defined at $t = 8.5$ ms, in Fig. 2(b). $R_{3,y}$ and $R_{3,x}$ are the larger and smaller droplet 3 radii, respectively. The hemiellipsoidal shape of droplet 3 is energetically unfavorable. Then, in the second stage of the coalescence process, droplet 3 relaxes to its equilibrium hemispherical shape of radius $R_{3,\mathrm{eq}}$. After this point, if a new droplet is printed at a distance d away from it, then the composite droplet becomes the "mother" droplet 1 and the cycle repeats itself. For each completed coalescence cycle, the center of mass of the resulting droplet 3 is translated by a certain distance from the point of origin, marked in red, in Figs. 2(a) and 2(b). The position of the new printed droplet 2 dictates the translation direction of droplet 1. Assuming that droplet 2 is printed laterally along the y axis, droplet 1 would be translated by a distance Δy from the point of origin, for each coalescence cycle, as is shown in Fig. 2(b) at $t = 106$ ms. (For more details on the evolution of the center of masses of these droplets, before and after coalescence, see Fig. S2 in the Supplemental Material [45].)

Figure 3(a) shows optical micrographs of the relaxation of droplet 3, and Fig. 3(b) reports the temporal evolution of $R_{3,y}$ and $R_{3,x}$. The relaxation of $R_{3,y}$ and $R_{3,x}$ to their equilibrium value $R_{3,\mathrm{eq}}$
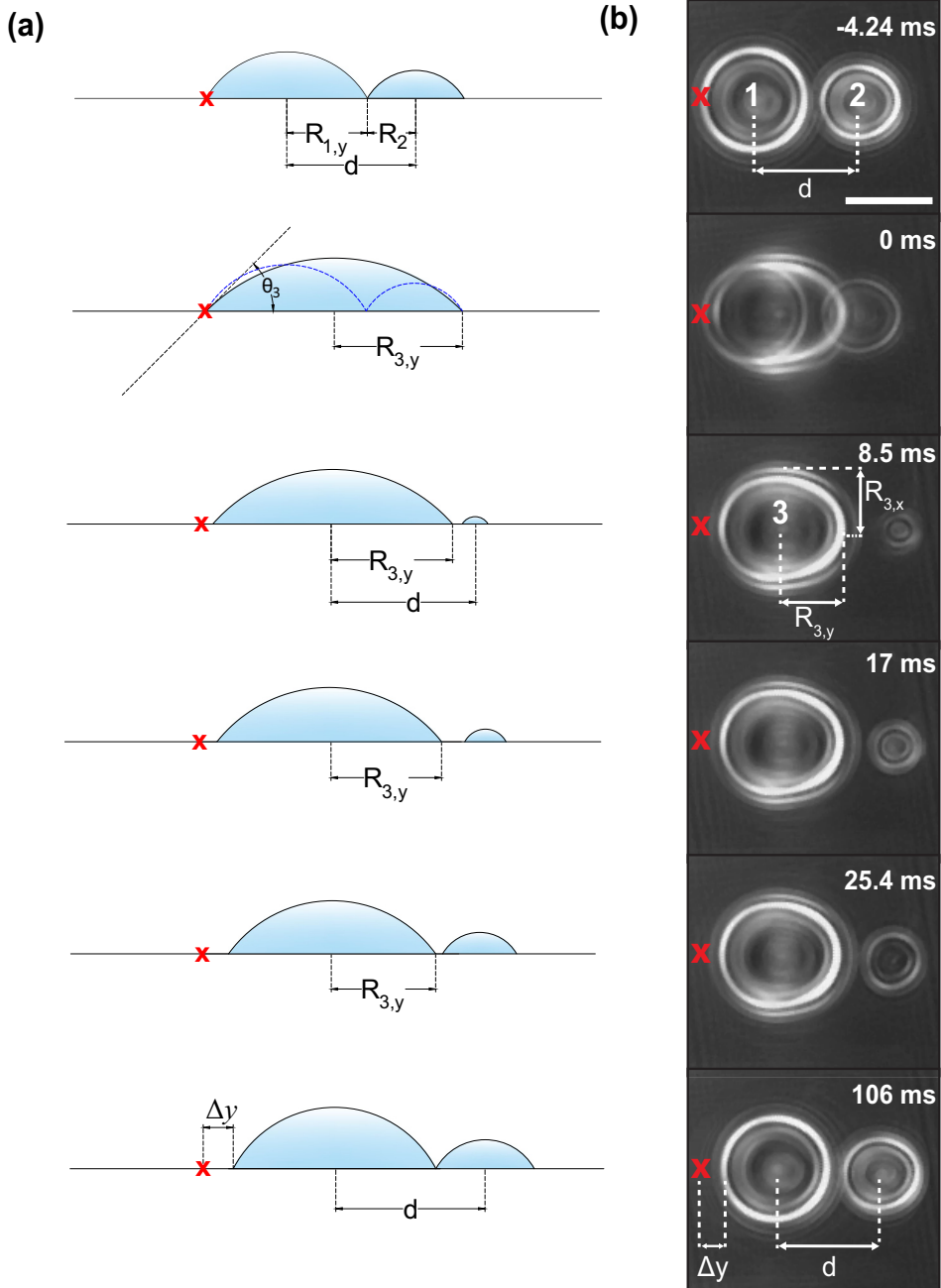
FIG. 2. Droplet movement initiation: droplets 1 and 2 coalesce to form a composite droplet 3, which in turn relaxes to a hemispherical cap shape, and is translated by a distance Δy as its contact line retracts, from the point of origin marked in red (and placed at the edge of the large radius $R_{1,y}$ of the mother droplet contact line), while a new droplet is growing at a distance d from it. The coalescence-induced dislocation of the composite droplet 3 is shown in the schematic illustrations in (a), from a side-view perspective, and in the optical micrographs in (b), from a bottom-view perspective. Scale bar: (b) 10 μm.
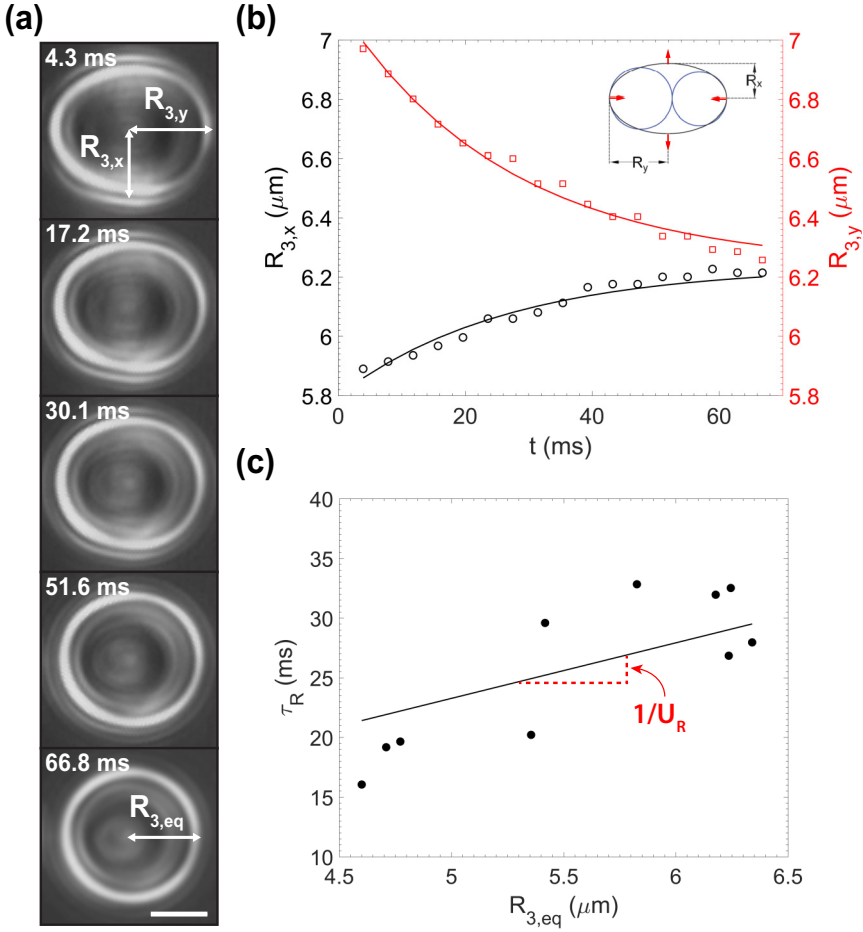
FIG. 3. (a) Optical microscope images showing the relaxation of the merged composite droplet from a hemiellipsoidal shape, right after coalescence, to its equilibrium spherical cap shape. (b) Time evolution of the composite droplet contact radii along the major (R_y) and minor (R_x) axes from one coalescence event. The curves are fits to Eqs. (1) and (2). The inset (upper right) shows a schematic of the coalescence of two sessile droplets viewed from the top; the red arrows denote the direction of liquid motion along the x and y axes. (c) Variation of the characteristic relaxation time, τ_R with the equilibrium droplet contact radius, $R_{3,eq}$ for ten coalescence events. The line is the best fit to Eq. (3). Scale bar: (a) 10 μm.

is exponential [40,51], and can be described by the equations [42]: $\dot{R}_{3,x} = \frac{R_{3,eq} - R_{3,x}}{\tau_R}$, and $\dot{R}_{3,y} = \frac{R_{3,eq} - R_{3,y}}{\tau_R}$, which have the following solutions, respectively:

$$R_{3,x}(t) = [R_{3,x}(0) - R_{3,eq}]e^{-(t/\tau_R)} + R_{3,eq}, \tag{1}$$

$$R_{3,y}(t) = [R_{3,y}(0) - R_{3,eq}]e^{-(t/\tau_R)} + R_{3,eq}, \tag{2}$$

where t is time, and τ_R is the characteristic relaxation time. The relaxation time τ_R for a given coalescence event is obtained by curve fitting Eqs. (1) and (2) to the data obtained from experiments, like that shown in Fig. 3(b). From Fig. 3(c), we can deduce that τ_R increases linearly with increasing equilibrium radius $R_{3,eq}$ of the droplet, in accordance with the results of other studies for water drops

TABLE I. Table of K values for liquid droplets of different sizes on rigid substrates.

Substrate	Liquid	Average droplet size (R_{eq}, μm)	K	References
Glass + silane	water	100–1000	$10^{-6} - 10^{-7}$	Andrieu *et al.* [40]
Silicon + silane	water	10–50	2.5×10^{-6}	Narhe *et al.* [41]
Glass + FDTS	PnB	5	2×10^{-5}	this study

[40,41,52], as well as for more viscous liquids such as diethylene glycol drops [53]. Hence we can write

$$\tau_R = \left(\frac{1}{U_R}\right) R_{3,\text{eq}}, \tag{3}$$

where the velocity U_R characterizes the relaxation rate of the receding contact line. U_R is not to be confused with the instantaneous contact line velocity, which varies during the relaxation process. The linear regression of the experimental data [solid line in Fig. 3(c)] yields a characteristic contact line relaxation rate of $U_R = 214 \pm 10 \, \mu\text{m s}^{-1}$. This value can be compared with the characteristic viscocapillary velocity for a droplet moving in a channel, which is defined as $U_V = \sigma/\mu$, where σ and μ are the droplet surface tension and viscosity, respectively [54]. For PnB (at 25 °C; $\sigma = 27.5$ mN/m, $\mu = 3.1$ mPa s [55]), $U_V = 8.9 \, \text{m s}^{-1}$, which is more than four orders of magnitude higher than U_R, the experimentally determined characteristic relaxation velocity of the coalescing PnB droplets studied here, mentioned earlier. This clearly implies that conventional hydrodynamic considerations alone cannot be used to describe the coalescence dynamics of sessile microdroplets in the partial wetting regime, and that the relaxation process is likely dominated by a dissipation wetting mechanism near the contact line.

Previous work has shown that the coalescence dynamics of sessile droplets is highly influenced by the presence of the solid surface and wetting effects. It has been shown theoretically that the application of the no-slip boundary condition on the solid surface leads to a diverging energy dissipation near the contact line region [56]. Several microscopic models have been proposed to describe partially wetting droplets contact line dynamics; however, no single theory for the underlying physical mechanism is universally accepted [57–62] (see also Supplemental Material Sec. I [45]). We note here that most of these models result in a general expression for the contact line velocity U_{CL} in a direction normal to the contact line, written as $U_{\text{CL}} = U_V K(\cos \theta_{\text{eq}} - \cos \theta)$, where θ is the dynamic contact angle, θ_{eq} is the equilibrium contact angle, and K is a model-dependent, dimensionless parameter that captures the effect of contact line dissipation. Small values of K mean that the dissipation in the contact line region is larger than that in the bulk of the liquid. Several experimental studies of droplet dynamics on rigid substrates have determined typical values of K to be 10^{-6} to 10^{-7} for water [40,41,52] (Table I). We have determined our value of K to obtain the maximum capillary forces driving the flow by $K \approx \frac{U_R}{U_V}\left(\frac{1}{\cos \theta_r - \cos \theta_a}\right)$, with the receding contact angle $\theta_r = 53.2°$ and the advancing contact angle $\theta_a = 71.4°$, and found it to be 8.5×10^{-5}. This value of K is of the same order of magnitude as that calculated based on an established theoretical model [51], for the relaxation of nonspherical sessile droplets on partially wetting surfaces, which yields $K \approx 2 \times 10^{-5}$, Table I (for detailed calculation, see Supplemental Material Sec. I [45]) [51]. Such a small K value clearly shows that, even for the minute droplets examined in this study, the dynamics of the droplet is limited by the dissipation in the vicinity of the contact line. This dissipation leads to a relaxation more than four orders of magnitude slower than that predicted by bulk hydrodynamics, which is in accordance with the K values of previous studies that looked at coalescence of sessile droplets, even of macroscopic sizes [40–42,52,53]. This indicates that contact line dynamics and dissipation near that are very important for describing droplet coalescence—and the overall motion of droplet 3—and therefore the resulting Pac-Man transport mechanism investigated here.
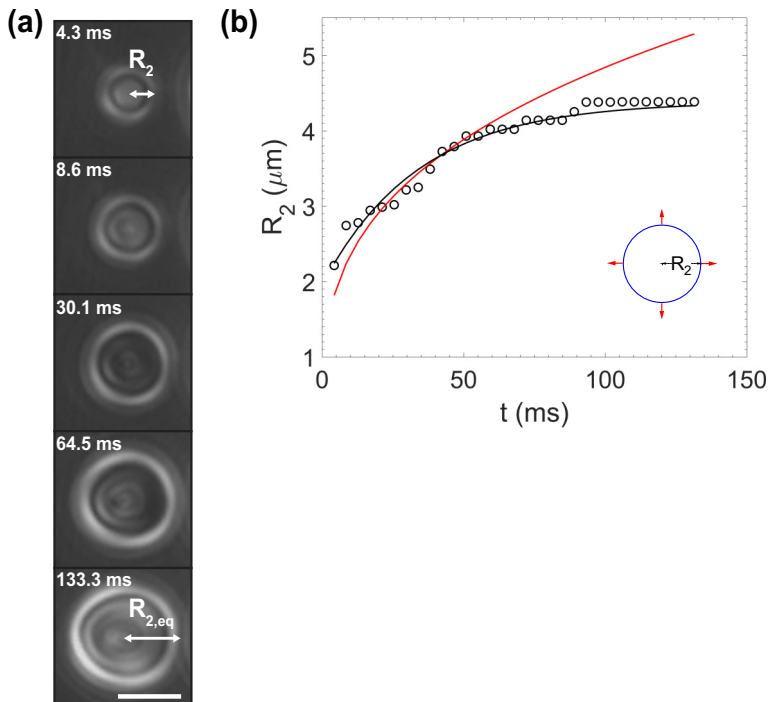
FIG. 4. (a) Optical microscope images showing the growth of the daughter droplet (droplet 2), with contact radius R_2, to its equilibrium size of radius $R_{2,\text{eq}}$. (b) Temporal evolution of the contact radius R_2 of droplet 2. The inset (lower right) shows a schematic of the growing droplet, with the red arrows denoting the direction of liquid motion along the x and y axes. The black curve is a fit to Eq. (4), and the red curve is a power law fit, such that $R_2 \sim t^{1/3}$. Scale bar: (a) 10 μm.

Similarly, we have investigated the dynamics of a single growing sessile microdroplet (here representing the daughter droplet), which grows due to continuous printing of additional smaller droplets [Fig. 1(a)]. The growing daughter droplet maintains a spherical cap shape, such that its contact radius $R_2 = R_{2,y} = R_{2,x}$, as can be seen in the optical micrographs in Fig. 4(a). Figure 4(b) reports the evolution of R_2 with time t. At the beginning of droplet printing, one can expect that the volume deposited grows linearly with time, such that the radial growth rate obeys a power law of $(R_2)^3 \sim t$, which translates to $R_2 \sim t^{1/3}$. This is shown by the power-law fit for times where we can neglect evaporation effects, as can be seen in Fig. 4(b). At later stages, evaporation effects become important, and the droplet-substrate contact radius starts to converge to an equilibrium size $R_{2,\text{eq}}$. To describe this behavior, we can write

$$R_2(t) = [R_2(0) - R_{2,\text{eq}}]e^{-(t/\tau_G)} + R_{2,\text{eq}}, \tag{4}$$

where τ_G is the characteristic growth time of the droplet. Figure 4(b) shows that the experimental data can be reasonably fitted with the exponential function (4). Previous theoretical and experimental work has also shown that spreading macroscopic droplets have a contact radius that grows exponentially [42,63].

For a given set of printing parameters, the droplet grows to a spherical cap equilibrium size of radius $R_{2,\text{eq}}$. Hence we can write $\tau_G = \frac{1}{U_G}R_{2,\text{eq}}$, where U_G is the corresponding characteristic growth rate of the droplet, for the present printing conditions, estimated to be $U_G = 129\,\mu\text{m s}^{-1}$. U_G should not be confused with the instantaneous contact line velocity of the growing droplet, which varies with time during the growth process, as also discussed earlier for the relaxation velocity U_R. In

fact, the growing droplet exhibits a rapid expansion during the early stage of its growth, as can be seen in Fig. 4(b), when the addition of each printed droplet contributes more significantly to the overall deposited volume on the substrate. Taking the derivative of the power law fit of $R_2 \sim t^{1/3}$ at early times, we find that in the first few milliseconds of its expansion, the daughter droplet has an instantaneous radial growth ranging from $\approx 975 \, \mu\text{m s}^{-1}$ (for $R_2 = 200$ nm) to $\approx 210 \, \mu\text{m s}^{-1}$ (for $R_2 = 2 \, \mu\text{m}$). From this, we can see that the advancing contact line speed of the printing droplet, when it is first being formed, can greatly exceed the receding contact line speed of the retracting droplet.

Once the printed droplet reaches its equilibrium size of radius $R_{2,\text{eq}}$, it maintains a quasistable volume where the printing ejection flow rate is exactly compensated by the liquid evaporation from the droplet (for calculation of the printing flow rate, see Supplemental Material Sec. IV [45]). This plateau in size can be seen in our measured data of the contact radius of the droplet, in Fig. 4(b), from around $t = 93$ ms onwards. In principle, the active volume stabilization of a single sessile droplet can be maintained as long as the printing actuation is on, as has been shown in a previous study [37]. Evaporation also plays a key role in our coalescence process, ensuring that the merged composite droplet maintains the same size after each coalescence event. For an averaged size droplet of contact radius 5 μm, we have calculated the volumetric evaporation rate of PnB to be on the order of $O(100 \, \mu\text{m}^3 \, \text{s}^{-1})$. For detailed calculations of the evaporation rate, see Supplemental Material Sec. III [45].

B. Omnidirectional planar movement of the self-propelled droplets

The movement of the self-propelled droplets is fueled by the continuous coalescence of the droplet pairs and can therefore be realized in any direction of the substrate. Next, we explore the limits of the droplet self-propulsion set by the available substrate (stage) velocity and by the size of the printed droplets themselves. Owing to the antifouling nature of the employed surface, we are able to reuse the same substrate for all of the experiments performed. We observed experimentally that there is a range of interdroplet separations d for which the bridging, and hence coalescence, of the mother and daughter droplets is possible. While the pipette nozzle dispensing the liquid is fixed, the distance d, measured from droplet center to center, is controlled by the underlying moving stage velocity. As the daughter droplet grows in size, coalescence will occur if it catches up with the retracting mother droplet, which is placed at a distance d from it. Hence bridging also depends on the sizes of droplets 1 and 2, given by their contact radii $R_{1,y}$ and R_2. Thus we can define the ratio $\frac{d}{R_{1,y}+R_2}$, which we measure experimentally, to predict the bridging between droplets 1 and 2.

Figure 5(a) shows optical micrographs of the droplets interacting with an increasing stage velocity from 0.001 to 0.1 mm s^{-1}. We have performed stage velocity-variation experiments multiple times in order to define the working range of stage velocities that result in coalescence. For stage velocities up to 0.02 mm s^{-1}, we observed that bridging and coalescence of the droplet pair occur continuously and in a reproducible periodic manner, as can be seen in Video S1 of the Supplemental Material [45], for a stage velocity of 0.018 mm s^{-1}. However, this is not the case at higher substrate speeds where an intermittency is observed and the result is a series of individually separated droplets. For every missed coalescence event, the individual droplets evaporate and leave behind solute residues they carried, as indicated by the white arrows in Fig. 5(a). Figure 5(b) summarizes the type of the droplet interaction outcome, coalescence or noncoalescence, for the different $\frac{d}{R_{1,y}+R_2}$ values measured from experiments. Each data point corresponds to one mother-daughter droplet experiment. These values are obtained by varying the stage velocity and measuring the corresponding interdroplet distances d, and droplet contact radii $R_{1,y}$ and R_2, for each completed or missed coalescence event. The faster the stage velocity is, the larger the interspacing d becomes, which translates into larger $\frac{d}{R_{1,y}+R_2}$ values, and lower occurrences of coalescence.

Further, based on our findings and modeling of the contact line relaxation and growth dynamics, we simulated the contact line motion at the limits where the droplets are closest, for a coalescing
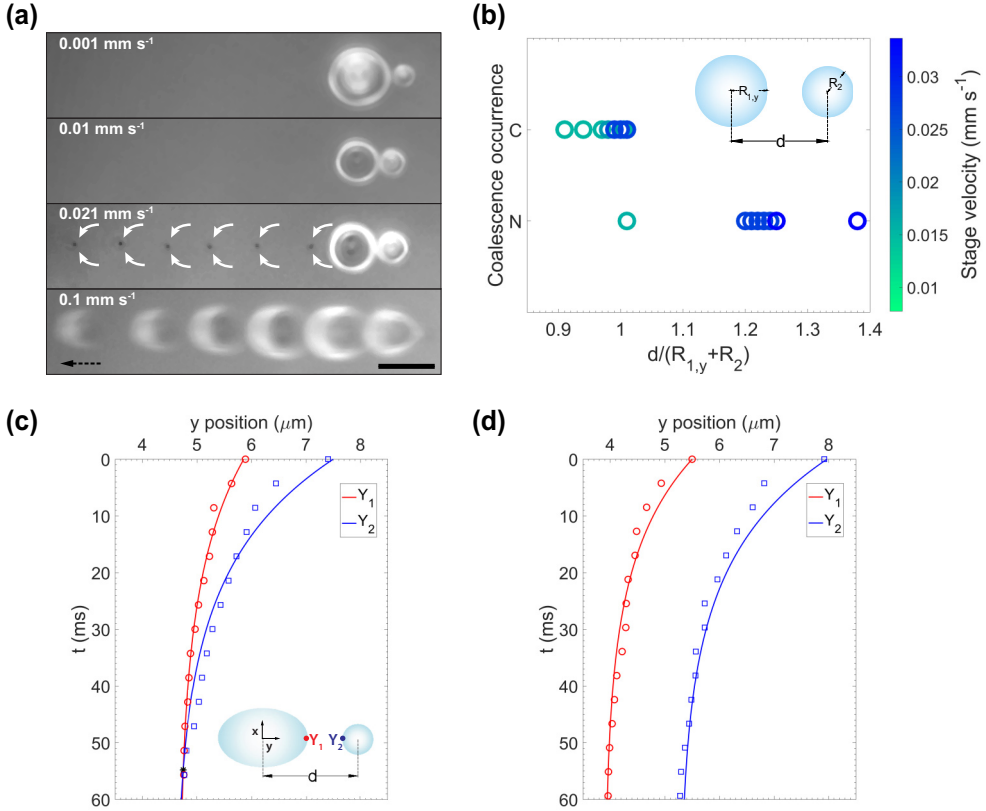
FIG. 5. (a) Optical micrographs showing droplet pairs interacting with a stage velocity of increasing magnitude, from 0.001 to 0.1 mm s^{-1}. As the stage velocity reaches 0.021 mm s^{-1}, an intermittency in coalescence events is observed. The white arrows indicate the solute residues left behind by single evaporated droplets that did not coalesce. At the bottom micrograph, one can observe a series of individually separated droplets, within a time frame (here, 40 ms), as the stage is translated at a relatively high velocity of 0.1 mm s^{-1}. (b) Plot showing the interaction type of two sessile droplets separated by a distance d, for a given stage velocity, with C = coalescence and N = noncoalescence. The distance d is measured center-to-center, as shown in the inset, and the value of $\frac{d}{R_{1,y}+R_2}$ is measured directly from experiments, for each coalescence and noncoalescence event. (c) Plot showing a simulation (solid line), and experimental data (symbols) of the change in the contact line positions Y_1 and Y_2 with time, for a coalescence event, with $\frac{d}{R_{1,y}+R_2} = 0.98$ and a stage velocity of 0.015 mm s^{-1}, (d) similarly for a non-coalescence event with $\frac{d}{R_{1,y}+R_2} = 1.2$ and a stage velocity of 0.025 mm s^{-1}. Scale bar: (a) 10 μm.

pair ($\frac{d}{R_{1,y}+R_2} = 0.98$; stage velocity $= 0.015$ mm s^{-1}), and farther apart, for a noncoalescing pair ($\frac{d}{R_{1,y}+R_2} = 1.2$; stage velocity $= 0.025$ mm s^{-1}). In the model, we solve Eqs. (1), (2), and (4), using the previously calculated characteristic growth and relaxation times, τ_G and τ_R, for different initial conditions extracted from experiments in Fig. 5(b). We did this to understand if we could predict a coalescence event based on our findings. Figures 5(c) and 5(d) show the positions of the contact lines in droplets 1 and 2, designated by the points $Y_1 = R_{1,y}$ and $Y_2 = d - R_{1,y}$, respectively. Based on our experimental observations, we assume a simulation time of 60 ms in both cases, which is a typical duration for a complete coalescence event. We also consider that the center of mass of
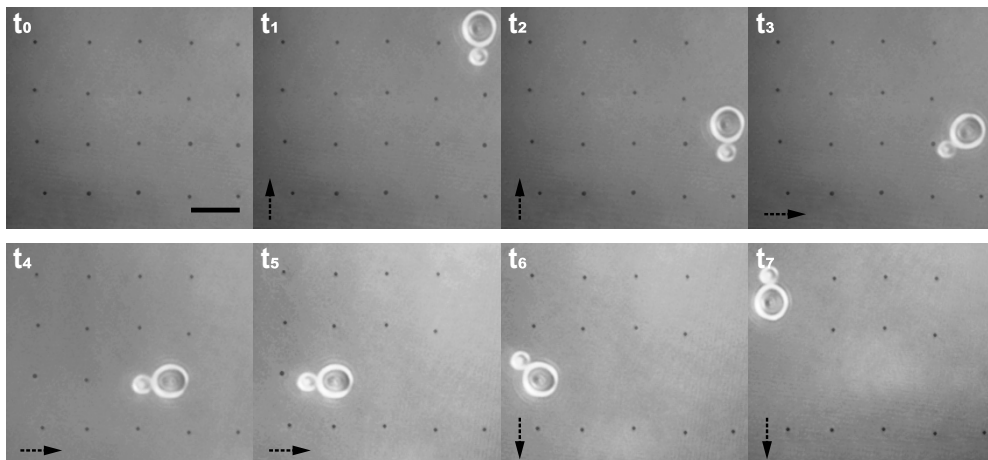
FIG. 6. Sequence of optical micrographs showing the self-propelled droplet collecting up an array of residues. At t_0, the array of residues is intact. From t_1 to t_7, the droplet pair is photographed picking up the solid particles, cleaning the surface along its way. The black arrows illustrate the movement of the nozzle-substrate axis. Scale bar:10 μm.

each parent droplet is stationary with respect to the underlying moving substrate (see Supplemental Material Fig. S2 [45]).

The results of the simulation are illustrated in Figs. 5(c) and 5(d) (solid curves) and compared against measured experimental data (symbols). For the coalescence case depicted in Fig. 5(c), the simulation predicts that the positions $Y1$ and $Y2$ overlap at precisely $t = 54.8$ ms, which is in good agreement with the measured experimental data, which shows an overlap at $t = 55.7$ ms. In Fig. 5(d), these two points do not meet, and hence coalescence does not occur. These results confirm the experimental findings of Fig. 5(b), where we do not expect coalescence events to occur for values of $\frac{d}{R_{1,y}+R_2}$ above unity. Thus, in order to have coalescence, the interspacing between droplets 1 and 2 needs to be sufficiently small such that the early exponential growth of the daughter droplet is exploited.

Using the concepts introduced above, and keeping in mind the set velocity limits, we demonstrate the performance, utility, and stability of the proposed system by controllably propelling microdroplets ($\sim$5 μm radii) over large distances, without intrinsic limits to their motion. Supplemental Material Video S1 [45] shows a close-up of the self-propelled droplets, for a stage velocity of 0.018 mm s^{-1}. The tunable omnidirectional movement of the droplets is displayed in Video S2 [45], which shows the self-propelled droplets traveling through a maze. The maze is lithographically prepatterned on the substrate, and the Pac-Man motion of the droplets is carried out in an instantaneous, on-demand manner. The trajectory of the droplets is digitally reconfigured, on the spot, simply by controlling the movement of the underlying stage. In addition, several droplets were made to navigate through the maze, often following the same route, which is a testament to the antifouling nature of this process and the reusability of the substrate.

Moreover, we task the self-propelled droplets to pick up, transport, and merge solid entities that are preprinted on the substrate, in an instantaneous, on-demand manner (see Supplemental Material Videos S3–S5 [45]). We also employ the droplet pair for subtractive patterning, or cleaning, of solid content, as illustrated in Fig. 6, and Video S3 [45]. To do so, we printed an array of solid particle groups, in order to mimic the effect of surface fouling by dirt particles. We then form a droplet doublet and proceed to move it on top of the array of deposits. We find that the deposits do not prohibit the movement of the droplets, but are rather picked up and carried along with them. The self-propelled droplets effectively clean the surface by ridding it of solid contaminants. The carried

particles are then combined and merged into a single entity "pile," inside the mother droplet. As the droplets continue to pick up the deposits in their way, the concentration of solid material in the mother droplet gradually increases. Eventually the amount of material accumulated becomes too large to transport, and effectively pins the contact line of the mother droplet, splitting the droplet doublet. This in turn prohibits droplet bridging and coalescence, causing the mother droplet to evaporate, and leave behind the entirety of the carried solid material it accumulated.

Taking this one step further, we task the self-propelled droplets to pick up and transport clusters of fluorescent nanoparticles, which we prepattern on the substrate. To do so, we first use a custom-made ink of CdSe-CdS core-shell nanocrystals dispersed in PnB to print microdiscs of fluorescent material on the substrate. Then, we create a droplet pair and move it above the fluorescent clusters. The self-propelled droplets are able to locally redissolve the nanoparticles and carry them along any given trajectory, as can be seen in Video S4 [45]. Furthermore, the droplet pair is able to mix and merge the nanoparticles it carries with other nanoparticle clusters already present on the substrate, hence creating small colloids on demand, as is shown in Video S5 [45]. Hence, this method served here as a tool to pick up, transport, and merge microscale solid entities at will, and in any given planar direction.

III. MATERIALS AND METHODS

Droplets were ejected by NanoDrip electrohydrodynamic printing onto a glass substrate coated with a self-assembled monolayer of 1H,1H,2H,2H-Perflurooctyltrichlorosilane (FDTS), and observed *in situ*, from below, by a home-built laser scanning microscope. Propylene glycol n-butyl ether (PnB) was employed as a solvent in the experiments, owing to its low vapor pressure and sufficiently high electrical conductivity.

Materials. In this study, we use borosilicate glass (BSG) substrates 200 μm in thickness obtained from Schlosser GmbH. For the chemical functionalization of the substrate surface, we use 1H, 1H, 2H, 2H-perfluorodecyltrichlorsilane (FDTS, 96%) from Alfa Aesar GmbH, hexane anhydrous (95%), and isopropyl alcohol (IPA) from Sigma-Aldrich, and deionized water purified from a Merck Milli-Q Direct Water Purification System. Propylene glycol n-butyl ether (PnB, $\geqslant$ 99%) was acquired from Sigma-Aldrich. We will use the PnB parameters at 25 °C: surface tension $\sigma = 27.5$ mN/m, and dynamic viscosity $\mu = 3.1$ mPa s [55].

Substrate preparation. We rendered the BSG substrates hydrophobic through a FDTS wet-chemistry treatment. To do so, we start by cleaning and activating all substrates by dipping them in a piranha solution for 10 min, and then rinsing them in DI water, and drying with a nitrogen gun. Subsequently, we immerse the samples in a mixture of 10 μL FDTS in 20 mL hexane for 2 min, followed by rinsing in hexane for 1 min, rinsing in IPA for 1 min, and rinsing in DI water for 1 min. Finally, we heat the substrates on a hotplate at 120 °C for 10 min.

We fabricated the maze and other metal markings on the substrates, prior to rendering them hydrophobic. To do so, we first sputter 50 nm of chromium onto cleaned BSG samples and then perform a standard photolithography step to transfer the desired patterns from a photomask, followed by a wet etching step in TechniEtch Cr01 (from MicroChemicals) to remove the undesired chromium.

Substrate characterization. We characterize the wettability of the FDTS-treated substrates by measuring the apparent equilibrium contact angle θ_{eq} of PnB via the sessile drop method, using a DataPhysics OCA 35 goniometer. Similarly, we measured the apparent advancing θ_a and receding θ_r PnB contact angles by inflating (advancing) and deflating (receding) ~ 1 μL of PnB with a microliter syringe.

Printing setup. The electrohydrodynamic printing setup consists of a liquid-laden glass capillary nozzle, an underlying piezostage, and an electrical actuation system. A confocal laser microscope (532 nm) is used for *in situ* optical detection of the droplets from below the glass sample. The printing setup components have been described in detail elsewhere [33]. The printing nozzles were prepared from borosilicate glass capillaries (World Precision Instruments, 1 mm outer diameter).

The capillaries were pulled to an outer diameter of 1.5–2 μm with a Sutter P-97 pipette puller, and then rendered conductive with an evaporated coating of 10 nm Ti and 100 nm Au. The capillary is back-filled with the PnB solvent and brought to a working distance between 10 and 15 μm of the glass substrate, which is mounted on a piezo stage, before a voltage is applied to actuate the printing process. The substrate is then moved by the underlying piezo stage at the desired set speed.

Electrohydrodynamic printing process. Droplets were stabilized by applying voltages in the range of 200–300 V between the PnB solvent situated in a gold-coated glass nozzle, and an indium tin oxide (ITO)-coated glass holder, situated below the substrate, and mounted on the piezo stage. Stable printing with continuous DC voltages was generally not possible, owing to the electrostatic charging of the nonconductive substrate. The charged sessile droplet led in turn to the deflection and repulsion of the incoming airborne droplets. To minimize these undesirable electrospraying effects, we applied an AC voltage signal consisting of short (500 μs) adjacent pulses of alternating polarity. Each pulse induces a controllable deformation of the liquid meniscus at the nozzle opening, and the ejection of a single droplet of approximately 33.5 aL (attoliter) in volume (corresponding to an airborne droplet of radius ≈ 200 nm). After polarity switching, a droplet of same volume and opposite charge is ejected, maintaining the charge neutrality of the accumulated sessile droplet. By having the printing actuation frequency equal to half the droplet ejection frequency, only one droplet per pulse polarity is ejected, efficiently avoiding any charging effects on the substrate. The natural ejection frequency of the droplets is maintained at ≈ 2 kHz, and the accumulated sessile droplet is sustained, as long as the applied electric potential is turned on. Details on the printing ejection frequency and flow rate can be found in Supplemental Material Sec. IV [45]. In all experiments, the pipette nozzle is fixed while the underlying substrate is moved.

IV. CONCLUSION

We exploited electrohydrodynamic nanoprinting to investigate an open-atmosphere microfluidic platform, where femtoliter sessile droplets can be formed sustainably despite high volatility, manipulated, and made mobile in any planar direction on-demand, by a continuous sequence of controlled coalescence events. Liquid evaporation also plays a key role in this mechanism, as it ensures that the merged droplet maintains a constant size after each coalescence cycle. Studying the coalescence kinetics of the sessile droplets in a partially wetting regime, we have found that, even for the minute sizes of the droplets studied, the contact line motion still dominates the process. The large dissipation near the contact line leads to a relaxation velocity close to five orders of magnitude slower than that predicted by bulk hydrodynamics. We also explore the limits of the coalescence-induced propulsion mechanism, and find that it is linked to a critical interspacing distance between the relaxing and evaporating mother and growing daughter droplets in an interacting pair, which we can control with the moving printing substrate velocity. Knowing the physics of our propulsion mechanism and its limits, we tasked the coalescing moving droplets to perform typical microfluidic operations such as collecting, transporting, and merging solid materials on otherwise unpatterned substrates.

experiments, designed the theoretical model, worked on the validation and reproducibility of the experiments, analyzed the data, and produced the figures. *Writing, original draft*: J.C., T.M.S., and D.P. wrote the initial draft of the paper. All authors have read and approved the final version of the paper.

---

[1] Y. H. Chang, G. Bin Lee, F. C. Huang, Y. Y. Chen, and J. L. Lin, Integrated polymerase chain reaction chips utilizing digital microfluidics, Biomed. Microdev. **8**, 215 (2006).

[2] R. Sista, Z. Hua, P. Thwar, A. Sudarsan, V. Srinivasan, A. Eckhardt, M. Pollack, and V. Pamula, Development of a digital microfluidic platform for point of care testing, Lab Chip **8**, 2091 (2008).

[3] Z. Hua, J. L. Rouse, A. E. Eckhardt, V. Srinivasan, V. K. Pamula, W. A. Schell, J. L. Benton, T. G. Mitchell, and M. G. Pollack, Multiplexed real-time polymerase chain reaction on a digital microfluidic platform, Anal. Chem. **82**, 2310 (2010).

[4] P. C. Gach, K. Iwai, P. W. Kim, N. J. Hillson, and A. K. Singh, Droplet microfluidics for synthetic biology, Lab Chip **17**, 3388 (2017).

[5] M. J. Jebrail and A. R. Wheeler, Digital microfluidic method for protein extraction by precipitation, Anal. Chem. **81**, 330 (2009).

[6] D. Chatterjee, B. Hetayothin, A. R. Wheeler, D. J. King, and R. L. Garrell, Droplet-based microfluidics with nonaqueous solvents and solutions, Lab Chip **6** 199 (2006).

[7] P. Y. Keng *et al.*, Micro-chemical synthesis of molecular probes on an electronic microfluidic device, Proc. Natl. Acad. Sci. USA **109**, 690 (2012).

[8] S. J. Maerkl, Integration column: Microfluidic high-throughput screening, Integr. Biol. **1**, 19 (2009).

[9] C. G. Yang, Z. R. Xu, and J. H. Wang, Manipulation of droplets in microfluidic systems, TrAC - Trends Anal. Chem. **29**, 141 (2010).

[10] R. Seemann, M. Brinkmann, T. Pfohl, and S. Herminghaus, Droplet based microfluidics, Rep. Prog. Phys. **75**, 016601 (2012).

[11] C. N. Baroud, F. Gallaire, and R. Dangla, Dynamics of microfluidic droplets, Lab Chip **10**, 2032 (2010).

[12] C. Liu, J. Sun, J. Li, C. Xiang, L. Che, Z. Wang, and X. Zhou, Long-range spontaneous droplet self-propulsion on wettability gradient surfaces, Sci. Rep. **7**, 7552 (2017).

[13] H. Mertaniemi, V. Jokinen, L. Sainiemi, S. Franssila, A. Marmur, O. Ikkala, and R. H. A. Ras, Superhydrophobic tracks for low-friction, guided transport of water droplets, Adv. Mater. **23**, 2911 (2011).

[14] J. B. Boreyko, P. Mruetusatorn, S. T. Retterer, and C. P. Collier, Aqueous two-phase microdroplets with reversible phase transitions, Lab Chip **13**, 1295 (2013).

[15] M. Abdelgawad and A. R. Wheeler, The digital revolution: A new paradigm for microfluidics, Adv. Mater. **21**, 920 (2009).

[16] M. H. Shamsi, K. Choi, A. H. C. Ng, and A. R. Wheeler, A digital microfluidic electrochemical immunoassay, Lab Chip **14**, 547 (2014).

[17] E. Samiei, M. Tabrizian, and M. Hoorfar, A review of digital microfluidics as portable platforms for lab-on a-chip applications, Lab Chip **16**, 2376 (2016).

[18] M. J. Jebrail, M. S. Bartsch, and K. D. Patel, Digital microfluidics: a versatile tool for applications in chemistry, biology and medicine, Lab Chip **12**, 2452 (2012).

[19] K. Choi, A. H. C. Ng, R. Fobel, and A. R. Wheeler, Digital microfluidics, Annu. Rev. Anal. Chem. **5**, 413 (2012).

[20] Q. Sun *et al.*, Surface charge printing for programmed droplet transport, Nat. Mater. **18**, 936 (2019).

[21] J. R. Millman, K. H. Bhatt, B. G. Prevo, and O. D. Velev, Anisotropic particle synthesis in dielectrophoretically controlled microdroplet reactors, Nat. Mater. **4**, 98 (2005).

[22] S. K. Fan, T. H. Hsieh, and D. Y. Lin, General digital microfluidic platform manipulating dielectric and conductive droplets by dielectrophoresis and electrowetting, Lab Chip **9**, 1236 (2009).

[23] T. P. Hunt, D. Issadore, and R. M. Westervelt, Integrated circuit/microfluidic chip to programmably trap and move cells and droplets with dielectrophoresis, Lab Chip **8**, 81 (2007).

[24] M. G. Pollack, R. B. Fair, and A. D. Shenderov, Electrowetting-based actuation of liquid droplets for microfluidic applications, Appl. Phys. Lett. **77**, 1725 (2000).

[25] J. Lee, H. Moon, J. Fowler, T. Schoellhammer, and C. J. Kim, Electrowetting and electrowetting-on-dielectric for microscale liquid handling, Sens. Actuators, A **95**, 259 (2002).

[26] S. K. Cho, H. Moon, and C. J. Kim, Creating, transporting, cutting, and merging liquid droplets by electrowetting-based actuation for digital microfluidic circuits, J. Microelectromech. Syst. **12**, 70 (2003).

[27] W. C. Nelson and C. J. C. Kim, Droplet actuation by electrowetting-on-dielectric (EWOD): a review, J. Adhes. Sci. Technol. **26**, 1747 (2012).

[28] Z. Long, A. M. Shetty, M. J. Solomon, and R. G. Larson, Fundamentals of magnet-actuated droplet manipulation on an open hydrophobic surface, Lab Chip **9**, 1567 (2009).

[29] Y. Zhang and N. T. Nguyen, Magnetic digital microfluidics - a review, Lab Chip **17**, 994 (2017).

[30] K. S. Khalil, S. R. Mahmoudi, N. Abu-Dheir, and K. K. Varanasi, Active surfaces: ferrofluid-impregnated surfaces for active manipulation of droplets, Appl. Phys. Lett. **105**, 041604 (2014).

[31] X. Ding *et al.*, Surface acoustic wave microfluidics, Lab Chip **13**, 3626 (2013).

[32] S. P. Zhang *et al.*, Digital acoustofluidics enables contactless and programmable liquid handling, Nat. Commun. **9**, 2928 (2018).

[33] P. Galliker, J. Schneider, H. Eghlidi, S. Kress, V. Sandoghdar, and D. Poulikakos, Direct printing of nanostructures by electrostatic autofocussing of ink nanodroplets, Nat. Commun. **3**, 890 (2012).

[34] S. J. P. Kress P. Richner, S. V. Jayanti, P. Galliker, D. K. Kim, D. Poulikakos, and D. J. Norris, Near-field light design with colloidal quantum dots for photonics and plasmonics, Nano Lett. **14**, 5827 (2014).

[35] J. Schneider, P. Rohner, D. Thureja, M. Schmid, P. Galliker, and D. Poulikakos, Electrohydrodynamic nanodrip printing of high aspect ratio metal grid transparent electrodes, Adv. Funct. Mater. **26**, 833 (2016).

[36] C. U. Hail, C. Höller, K. Matsuzaki, P. Rohner, J. Renger, V. Sandoghdar, D. Poulikakos, and H. Eghlidi, Nanoprinting organic molecules at the quantum level, Nat. Commun. **10**, 1880, (2019).

[37] P. Galliker, J. Schneider, L. Ruthemann, and D. Poulikakos, Open-atmosphere sustenance of highly volatile attoliter-size droplets on surfaces, Proc. Natl. Acad. Sci. USA **110**, 13255 (2013).

[38] D. G. A. L. Aarts, H. N. W. Lekkerkerker, H. Guo, G. H. Wegdam, and D. Bonn, Hydrodynamics of Droplet Coalescence, Phys. Rev. Lett. **95**, 164503 (2005).

[39] J. Eggers, J. R. Lister, and H. A. Stone, Coalescence of liquid drops, J. Fluid Mech. **401**, 293 (1999).

[40] C. Andrieu, D. A. Beysens, V. S. Nikolayev, and Y. Pomeau, Coalescence of sessile drops, J. Fluid Mech. **453**, 427 (2002).

[41] R. Narhe, D. Beysens, and V. S. Nikolayev, Contact line dynamics in drop coalescence and spreading, Langmuir **20**, 1213 (2004).

[42] R. Narhe, D. Beysens, and V. S. Nikolayev, Dynamics of drop coalescence on a surface: the role of initial conditions and surface properties, Int. J. Thermophys. **26**, 1743 (2005).

[43] R. D. Narhe, D. A. Beysens, and Y. Pomeau, Dynamic drying in the early-stage coalescence of droplets sitting on a plate, Europhys. Lett. **81**, 46002 (2008).

[44] M. Sellier and E. Trelluyer, Modeling the coalescence of sessile droplets, Biomicrofluidics **3**, 022412 (2009).

[45] See Supplemental Material at http://link.aps.org/supplemental/10.1103/PhysRevFluids.5.123602 for videos of the self-propelling droplets and further technical and theoretical details of the experiments, which include Refs. [31,37,46–51], and [57–60].

[46] V. S. Nikolayev, Dynamics and depinning of the triple contact line in the presence of periodic surface defects, J. Phys.: Condens. Matter **17**, 2111 (2005).

[47] P.-G. de Gennes, F. Brochard-Wyart, and D. Quéré, *Capillarity and Wetting Phenomena: Drops, Bubbles, Pearls, Waves* (Springer, New York, 2004).

[48] R. G. Picknet and R. Bexon, The evaporation of sessile or pendant drops in still air, J. Colloid Interface Sci. **61**, 336 (1976).

[49] G. McHale, S. M. Rowan, M. I. Newton, and M. K. Banerjee, Evaporation and the wetting of a low-energy solid surface, J. Phys. Chem. B **102**, 1964 (1998).

[50] R. Zargar, N. Shahidzadeh-Bonn, M. Aytouna, J. Eggers, D. Bonn, M. Habibi, and O. Carrier, Evaporation of water: evaporation rate and collective effects, J. Fluid Mech. **798**, 774 (2016).

[51] V. S. Nikolayev and D. A. Beysens, Relaxation of nonspherical sessile drops towards equilibrium, Phys. Rev. E **65**, 046135 (2002).

[52] X. Jiang, B. Zhao, and L. Chen, Sessile microdrop coalescence on partial wetting surfaces: effects of surface wettability and stiffness, Langmuir **35**, 12955 (2019).

[53] D. A. Beysens and R. D. Narhe, Contact line dynamics in the late-stage coalescence of diethylene glycol drops, J. Phys. Chem. B **110**, 22133 (2006).

[54] T. M. Squires and S. R. Quake, Microfluidics: fluid physics at the nanoliter scale, Rev. Mod. Phys. **77**, 977 (2005).

[55] DOWANOL^{TM} PnB, Prod. information, Form No. 110-00616-0304 (2004).

[56] C. Huh and L. E. Scriven, Hydrodynamic model of steady movement of a solid/liquid/fluid contact line, J. Colloid Interface Sci. **35**, 85 (1971).

[57] T. D. Blake and J. M. Haynes, Kinetics of liquid liquid displacement, J. Colloid Interface Sci. **30**, 421 (1969).

[58] A. Prevost, E. Rolley, and C. Guthmann, Thermally Activated Motion of the Contact Line of a Liquid ^{4}He Meniscus on a Cesium Substrate, Phys. Rev. Lett. **83**, 348 (1999).

[59] E. Rolley and C. Guthmann, Dynamics and Hysteresis of the Contact Line between Liquid Hydrogen and Cesium Substrates, Phys. Rev. Lett. **98**, 166105 (2007).

[60] Y. Pomeau, Représentation de la ligne de contact mobile dans les équations de la mécanique des fluides, C. R. Acad. Sci. - Ser. IIb, Mec. **328**, 411 (2000).

[61] F. Brochard-Wyart and P.-G. de Gennes, Dynamics of partial wetting, Adv. Colloid Interface Sci. **39**, 1 (1992).

[62] D. Bonn, J. Eggers, J. Indekeu, and J. Meunier, Wetting and spreading, Rev. Mod. Phys. **81**, 739 (2009).

[63] F. Rieutord, O. Rayssac, and H. Moriceau, Spreading dynamics of water droplets, Phys. Rev. E **62**, 6861 (2000).